The Modulation Effect of Transverse, Antibonding, and Higher-Order Longitudinal Modes on the Two-Photon Photoluminescence of Gold Plasmonic Nanoantennas

Wei-Liang Chen,[†,⊥] Fan-Cheng Lin,[‡,⊥] Yu-Yang Lee,[†] Feng-Chieh Li,[†] Yu-Ming Chang,[†] and Jer-Shing Huang[‡,§,*]

[†]Center for Condensed Matter Sciences, National Taiwan University, Taipei 10617, Taiwan, and [‡]Department of Chemistry and [§]Frontier Research Center on Fundamental and Applied Sciences of Matters, National Tsing Hua University, Hsinchu 30013, Taiwan. [⊥]These authors contributed equally to this work.

ABSTRACT Plasmonic nanoantennas exhibit various resonant modes with distinct properties. Upon resonant excitation, plasmonic gold nanoantennas can generate strong two-photon photoluminescence (TPPL). The TPPL from gold is broadband and depolarized, and may serve as an ideal local source for the investigation of antenna eigenmodes. In this work, TPPL spectra of three arrays of single-crystalline gold nanoantennas are comprehensively investigated. We carefully compare the TPPL spectra with dark-field scattering spectra and numerically simulated spectra. We show the modulation effect of the transverse resonant mode and the nonfundamental longitudinal mode on the TPPL spectrum. We also demonstrate suppression of TPPL due to the subradiant antibonding modes and study the influence of antenna resonant modes on the overall TPPL yield. Our work provides direct experimental evidence on nanoantenna-mediated near-to-far-field energy coupling and gains insight into the emission spectrum of the TPPL from gold nanoantennas.

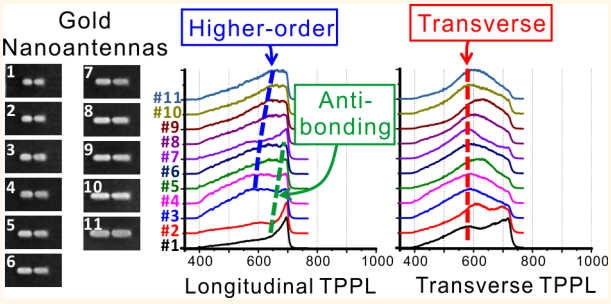

KEYWORDS: nanoantennas · plasmonic resonance · two-photon photoluminescence · dark mode

Plasmonic optical nanoantennas have been actively investigated because of their unique ability to mediate near- and far-field electromagnetic (e.m.) energy and to enhance nanoscale light–matter interaction.[1,2] Depending on the current distribution, a resonant plasmonic nanoantenna can be subradiant or superradiant,[3−10] and the emission polarization can be very different. The distinct property of the resonance mode in operation then determines the actual function of a nanoantenna in light–matter interaction. For example, the bonding modes of a symmetric gap nanoantenna can enhance excitation of dye molecules[11−13] because the bonding modes couple efficiently to linearly polarized far-field plane waves at resonant frequency. The bonding modes also provide efficient radiative decay channels for local sources to emit to the far field and are considered to be bright or super-radiant.[10] On the other hand, the antibonding mode exhibits completely out-of-phase currents on the two antenna arms and, therefore, does not efficiently couple to far-field electromagnetic waves. As a result, the antibonding modes cannot be excited efficiently by normally incident plane waves and the energy stored in the antibonding resonance does not decay into far-field radiation. The lack of radiative loss makes a nanoantenna in antibonding resonance a good nanoresonator with a relatively large quality factor compared to antenna in radiative bonding resonance. Therefore, the antibonding mode is suitable for plasmon-enhanced spectroscopy that requires high local field intensity.[14,15] Since the antibonding mode of a symmetric nanoantenna is

* Address correspondence to jshuang@mx.nthu.edu.tw.

Received for review May 1, 2014 and accepted August 28, 2014.

Published online September 10, 2014
10.1021/nn502389s

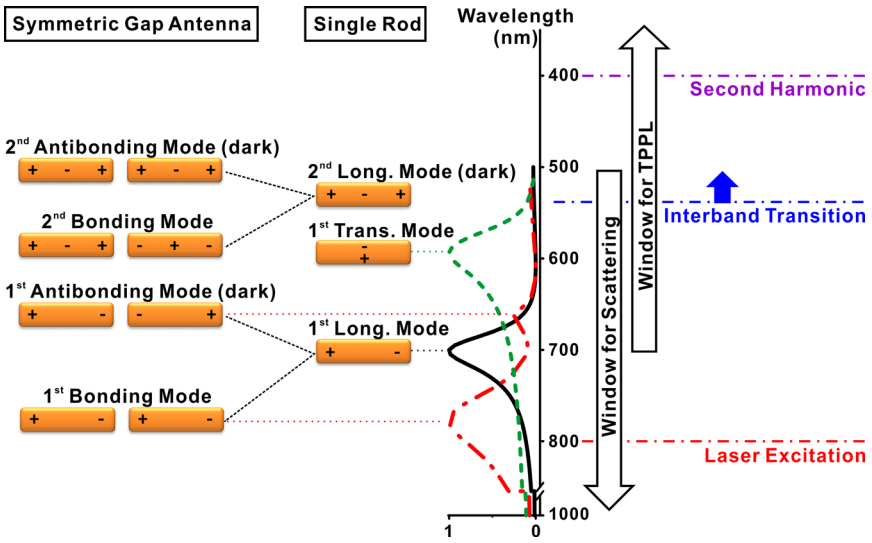

Figure 1. Energy-level diagram for the resonant eigenmodes of a symmetric gap nanoantenna and the corresponding single gold nanorod. The energy levels are plotted according to the simulated resonant spectra (middle panel) of the second nanoantenna in array C (height, width, total length = 30, 50, 216 nm, red dashed-dotted line) and the corresponding single nanorod (height, width, length = 30, 50, 100 nm, black solid line). For this nanoantenna, the transverse resonance (green dotted line) is very close to the second bonding mode. As the antenna length increases, the second bonding mode red-shifts to lower energy but the transverse resonance keeps its spectral position. Laser excitation, onset of the interband transition of gold material and the second harmonic of the laser are marked with red, blue, and purple dash-dotted lines on the right, respectively. The observation energy windows for the TPPL and the scattering spectra are indicated with thick open arrows.

optically dark, the electron beam is commonly used as an excitation source,[3,5,9] and the electron energy-loss spectroscopy is used in spatial and spectral analysis. For optical excitation of the antibonding mode, it is required that the symmetry of the excitation sources be broken because the structure is symmetric. This can be achieved by tilting the incident angle of the plane waves[4,8] or by displacing the laser focal spot from the symmetry center of the antenna.[6]

When gold nanoantennas are resonantly excited, the highly enhanced local field can promote the generation of two-photon photoluminescence (TPPL).[16−23] The TPPL of gold stems from sequential absorption of two photons followed by recombination of an electron in the sp band and a hole in the d band.[17,21] The absorption of the first photon regards an intraband transition and requires high field gradient to match the momentum.[16,17,21] Therefore, the generation of TPPL is sensitive to the local field intensity. Such sensitivity makes TPPL suitable for mapping the spatial distribution of antenna modes.[6,24] Since the TPPL from gold nanoantenna is broadband and strongly depolarized,[19] it serves as an ideal near-field light source for the spectral analysis of antenna eigenmodes.[16] Recently, Wissert *et al.* have studied the influence of the antenna resonance on the TPPL spectrum.[18,20] They showed that the TPPL spectrum is shaped by the antenna's fundamental bonding modes. Such modulation effect of antenna bonding modes has also been observed in the spectrum of one-photon photoluminescence from gold nanodisks.[25−27] These results suggest that the local energy of photoluminescence can relax into far-field emission *via* the antenna's fundamental bright mode.

In principle, the local e.m. energy can also decay into other resonant modes, such as higher-order bonding modes or subradiant antibonding modes. The spectral modulation effect on the TPPL spectra due to the higher-order bonding and subradiant antibonding modes has not been reported. To observe the influence of fundamental bonding resonance on the TPPL, the excitation wavelength must be red-shifted from the bonding resonance such that the excitation can be spectrally filtered out.[18] Differently, for the antibonding and higher-order bonding resonance, the use of excitation in resonance with the bonding mode is not an issue. The reason is that the spectral positions of the antibonding mode and the higher-order bonding modes are naturally blue-shifted from that of the fundamental bonding mode. Such blue shift makes it possible to observe the higher-order bonding mode and fundamental antibonding mode in the visible spectral window with resonant excitation in the NIR regime. Figure 1 depicts the energy diagram of a symmetric gap nanoantenna and the corresponding single nanorod.

In this work, we comprehensively study the influence of various resonant modes on the excitation and emission of TPPL from high-definition single-crystalline gold nanoantennas. In particular, we report the first experimental evidence for the modulation effect of the higher-order bonding mode and the subradiant

TABLE 1. Nominal Dimensions of the Fabricated Symmetric Gold Nanoantenna Arrays

	gap (nm)	height (nm)	width (nm)	total length (nm)	aspect ratio (total length/width)	number of antennas
array A	20	50	100	220−340, ΔL = 20 nm	2.2−3.4	7
array B	16	30	70	196−396, ΔL = 20 nm	2.8−5.7	11
array C	16	30	50	196−396, ΔL = 20 nm	3.9−7.9	11

antibonding mode on TPPL. Three arrays of gold nanoantennas with different widths are fabricated and investigated. Both linear scattering and TPPL spectra from single nanoantennas are investigated for both transversal and longitudinal polarization directions. Being able to observe and identify the effect of nonfundamental antenna modes on the TPPL spectrum not only helps understand the spectral shape of the TPPL emission spectrum but also gains insight into the flow of local e.m. energy into difference resonant eigenmodes of a nanoresonator. Using the self-generated TPPL as local broadband e.m. source, the eigenmode analysis can be performed at the nanostructure's local environment. This is particularly useful for *in situ* characterization of functional nanostructures in complex nanonetworks, for example a nanoantenna in a plasmonic optical nanocircuit. The fact that TPPL couples to the dark resonance modes also suggests a new way to inject e.m. energy to the dark modes.

RESULTS AND DISCUSSION

Nanoantenna Fabrication. Single-crystalline nanoantennas are fabricated by applying focused-ion beam (FIB) milling into chemically grown gold flakes drop-casted on top of an indium tin oxide (ITO) layer coated on a microscope cover glass.[28] This hybrid method minimizes the fabrication uncertainty and thus the signal fluctuation due to rough surface and random crystal grains. Although the quality of nanoantennas is improved, the edges of the nanoantennas are still rounded due to the sputtering process of the gallium-ion beam. Recently, helium-ion beam lithography has been applied to further improve the critical geometrical features of plasmonic nanoantennas, such as the gap size and the sharpness of the edges.[29,30] Although, FIB milling into the single-crystalline gold flakes can possibly damage the crystal lattice, the amorphous layer is less than 1 nm and the optical properties of nanoantennas are still superior compared to the multicrystalline ones.[28] In this work, the antennas in one array have nominally identical width, height, and similar geometry of the arm edges and gap. The only scanned parameter within one array is the total length of the nanoantenna. It is worth noting that being able to fabricate high-definition nanoantennas is important for the successful observation of the weak effects from the dark and higher-order bright modes with only one antenna array. Table 1 summarizes the dimensions of the three nanoantenna arrays.

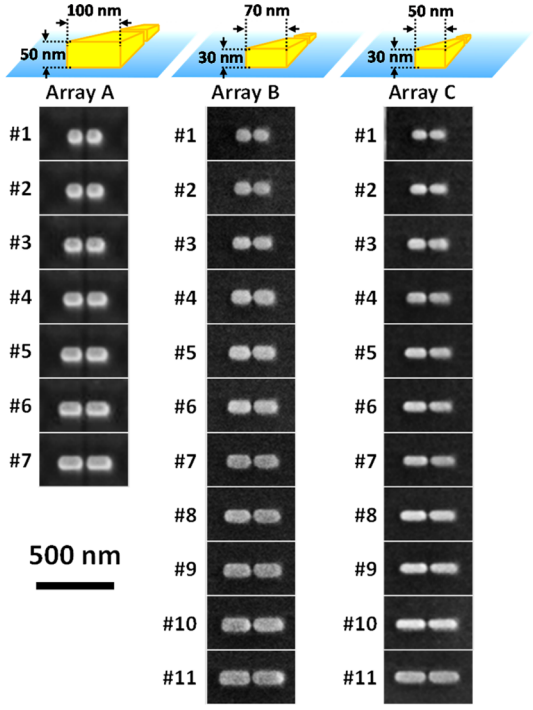

Figure 2. Scanning electron microscope images of single-crystalline gold nanoantennas in the three arrays. The scale bar of 500 nm applies to all images. Inset on top of each column depicts the cross sectional area of the nanoantennas in the corresponding array.

The scanning electron microscope (SEM) images of the three nanoantenna arrays are shown in Figure 2. The images for the full flake area are shown in Figure S1 (Supporting Information). We note that the variation in the local environment is larger with FIB milling compared to e-beam lithography because FIB milling also removes the substrate. In all our simulations, we have taken into account the local shape of the substrate. Around the antenna, the 40 nm thick ITO layer is milled away. In principle, measuring duplicates of antenna would help to minimize the signal fluctuation due to variation in the local environment. However, the size of our flakes does not allow us to fabricate enough number of duplicates for all the nanoantenna arrays. Therefore, we have optimized the FIB milling sequence to minimize the variation of the local environment. All nanoantennas in one array have been fabricated in one single batch with identical FIB condition and milling sequence. The FIB sequence is also designed in such a way that the distance from the antenna edges to the unmilled area is kept constant for all antennas (1000 nm). With such a distance larger than one

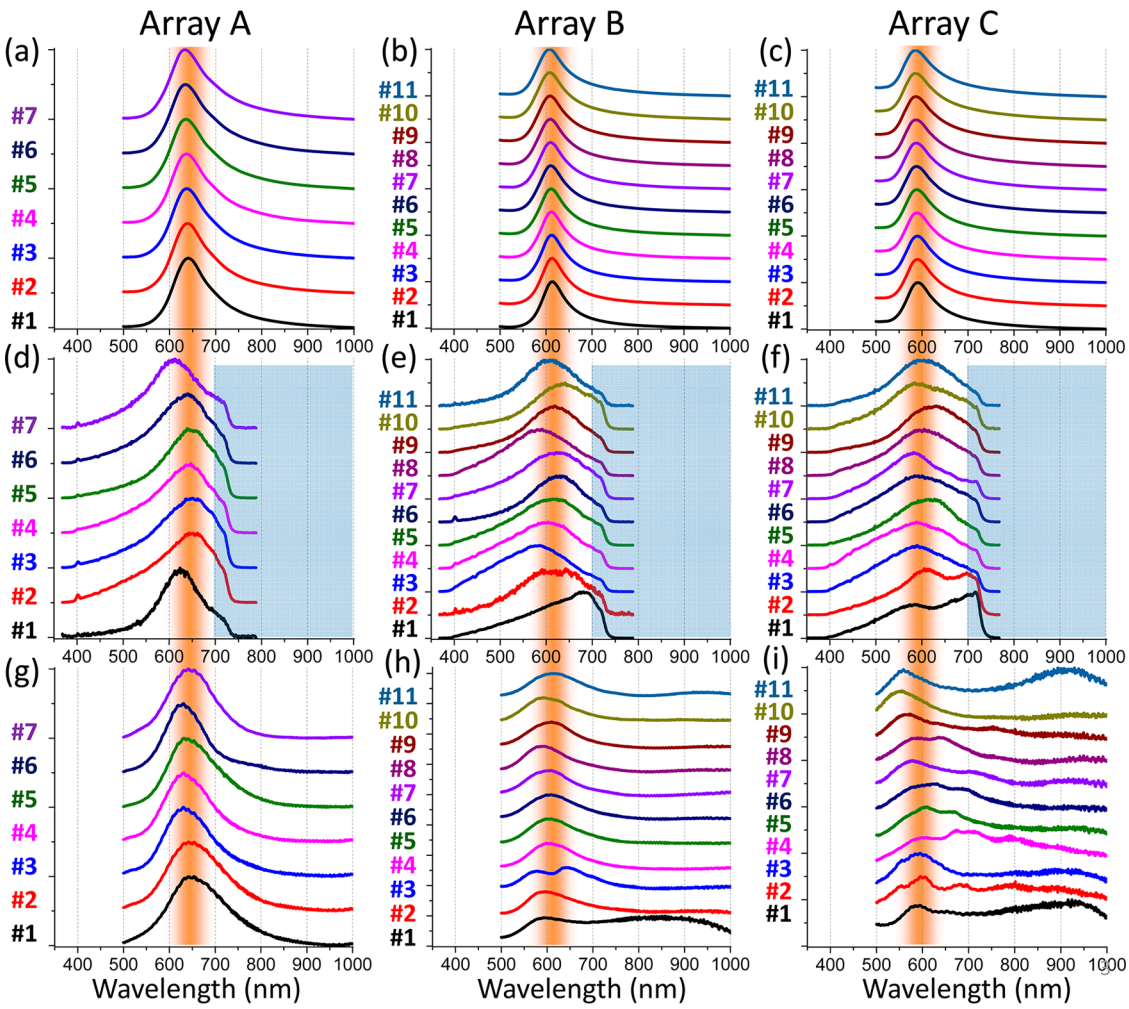

Figure 3. Normalized transverse resonance spectra of all nanoantennas in the three arrays obtained from simulated far-field scattering spectra (a−c), experimental TPPL emission spectra (d−f), and experimental dark-field scattering signals (g−i).The gradient orange area in each column marks the spectral position of the simulated transverse resonance. The gray areas in (d−f) are the spectral regime blocked by the short pass filter.

vacuum wavelength, the influence of geometrical variation at the border of milled and unmilled areas can be neglected. In addition, the distance from one antenna to the neighboring ones is about 2000 nm, which minimizes the cross talk of neighboring antennas.

Influence of Transverse Resonant Eigenmodes on the TPPL Spectra. We first examine the influence of the transverse resonant eigenmodes on the TPPL spectra. For this purpose, the polarizer has been rotated to select the TPPL emission with polarization perpendicular to the antenna's longitudinal axis. The polarization of the excitation is parallel to the antenna's longitudinal axis. Since TPPL from gold is strongly depolarized,[19] the local energy can decay into far-field photons through the transverse dipolar resonant modes of the nanoantenna, leading to a modulation of transverse TPPL spectrum. Figure 3 shows the transverse spectra for the three antenna arrays obtained from FDTD simulations (Figures 3a−c), TPPL experiment (Figures 3d−f), and dark-field scattering experiment (Figures 3g−i). The transverse TPPL and scattering spectra clearly show spectral peaks enhanced by the transverse resonance of the nanoantennas. The peak position is also in good agreement with the simulated data. The resonant wavelengths obtained from the transverse TPPL spectra for antenna array A, B, and C are 636 ± 14 nm, 614 ± 30 nm, and 599 ± 18 nm, respectively. The simulated values of the transverse resonance for antenna array A, B, and C are 635, 615, and 595 nm, respectively.

Since the "plasmon length"[31] of the transversal antenna cavity is determined by the width of the nanoantennas, the transverse resonant wavelength scales with the antenna width and the peak position in the transverse TPPL emission spectrum red-shifts with increasing antenna width. In Figure 4, we plot the wavelength of the transverse resonances obtained in this work as a function of antenna width, which determines the transverse cavity length. Data points from previous work[20] are also included. Error bars are added to Figure 4 in order to indicate the uncertainty. The plot shows clear dependence of the wavelength of

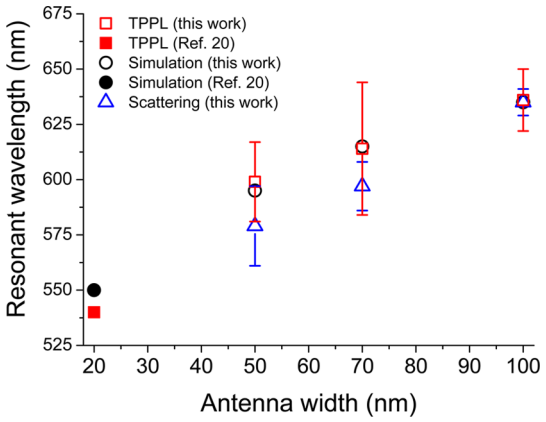

Figure 4. Resonant wavelength of the transverse antenna mode obtained from numerical simulations (black open circles), from experimental TPPL spectra (red open squares), and from experimental scattering spectra (blue open triangles) with respect to the antenna width. Error bars indicate the standard deviation within one antenna array. The simulated (black solid dot) and experimental (red solid triangle) data from ref 20 are also included.

the transverse resonance on the antenna width, as predicted by the cavity model.[2,32] In fact, the height of the antenna also influences the transverse resonance peak position. Increasing the height of the antenna increases the length of the out-of-plane transversal antenna cavity and, therefore, red-shifts the out-of-plane transverse resonance. In our experiment, the height of the nanoantennas in one array is identical and is determined by the thickness of the chemically synthesized gold flake. Since array B and array C are fabricated on the same flake, the height of the antennas in these two arrays is the same, and the difference in the transverse resonance positions should purely come from the different width. As for array A, both the height and the width are changed. Therefore, both dimensions are responsible for the difference in the transverse resonance. This experimental evidence that transverse TPPL is modulated by the transverse resonance of the nanoantenna demonstrates the ability of the nanoantenna to mediate the local e.m. energy to the far field and reveals the depolarized nature of TPPL from gold.

In this work, nanoantennas in the same array are nominally the same in width and height. Therefore, they are expected to show very similar transverse resonance. Nevertheless, fluctuation of the transverse resonance wavelength for nanoantennas in the same array is still observed due to geometrical uncertainty of the fabricated structure. Although our single-crystalline nanoantennas are relatively well-defined,[28] there is inevitable uncertainty in the fabricated structures. It is worth noting that each spectrum in our data is obtained from measuring only one single antenna at its local environment. This means that the influence of any local variation is revealed in the spectrum. This is very different from measuring the overall spectral response of a group of identical antennas, in which the individual difference is averaged out. Such fluctuation of the peak position, in fact, points out that a single nanoantenna is just like a single molecule, whose spectral response is unique and local environment-dependent. In principle, the optical response of any nanostructures in a complex nanonetwork, for example, a nanoantenna in an optical nanocircuit, should be characterized *in situ* and individually in order to reveal the true optical property of each nanodevice at its local environment. For such a purpose, the self-generated TPPL would be a good source for *in situ* characterization of optical nanostructures.

Influence of Longitudinal Resonant Eigenmodes on the TPPL Spectra. Next, we examine the modulation of TPPL spectrum due to the longitudinal resonant eigenmodes. Here, the polarizer is rotated to select the TPPL emission with polarization parallel to the antenna's longitudinal axis. The polarization of the excitation is still parallel to the antenna's longitudinal axis. Figure 5 panels a–c show the simulated near-field spectra for all nanoantennas in the three arrays. Figure 5 panels d-f and Figure 5 panels g–i show the experimental spectra for the TPPL emission and dark-field scattering, respectively. Figure 5 panels j–l show the simulated longitudinal scattering spectra of all the antennas. In the simulated near-field spectra, resonance peaks for the fundamental bonding mode, fundamental antibonding mode, and the first higher-order bonding mode are clearly seen. Differently, the peaks for antibonding mode are missing in the simulated far-field spectra shown in Figure 5j–l. This is because the excitation source used in the far-field scattering simulations is a normally incident plane wave source which does not couple to the antibonding mode.[6] All longitudinal resonances gradually red shift as the antenna length increases. It is worth noting that the antibonding mode exhibits a smaller peak width than the bonding mode, revealing the reduced radiative damping and higher quality factor of the subradiant antibonding mode. Therefore, the TPPL energy that decays into the antibonding mode would be stored in the near field for a longer time and eventually dissipate into heat instead of far-field emission, resulting in a "dip" in the TPPL spectrum due to the suppression of emission. As marked by the green dashed lines in Figure 5(d)-(f), spectral dips in TPPL emission are observed. The positions of the dips well correlate to that of the antibonding mode in the simulated spectra and the scattering spectra. As for higher-order bonding modes, they are bright but the emission efficiency is much lower compared to that of the fundamental bonding modes, resulting in weak enhancement in the blue-shifted spectral regime. As indicated by the blue dashed lines in Figure 5d–f, the TPPL spectra show slightly enhanced intensity around spectral position of the higher-order bonding mode. The wavelengths of the

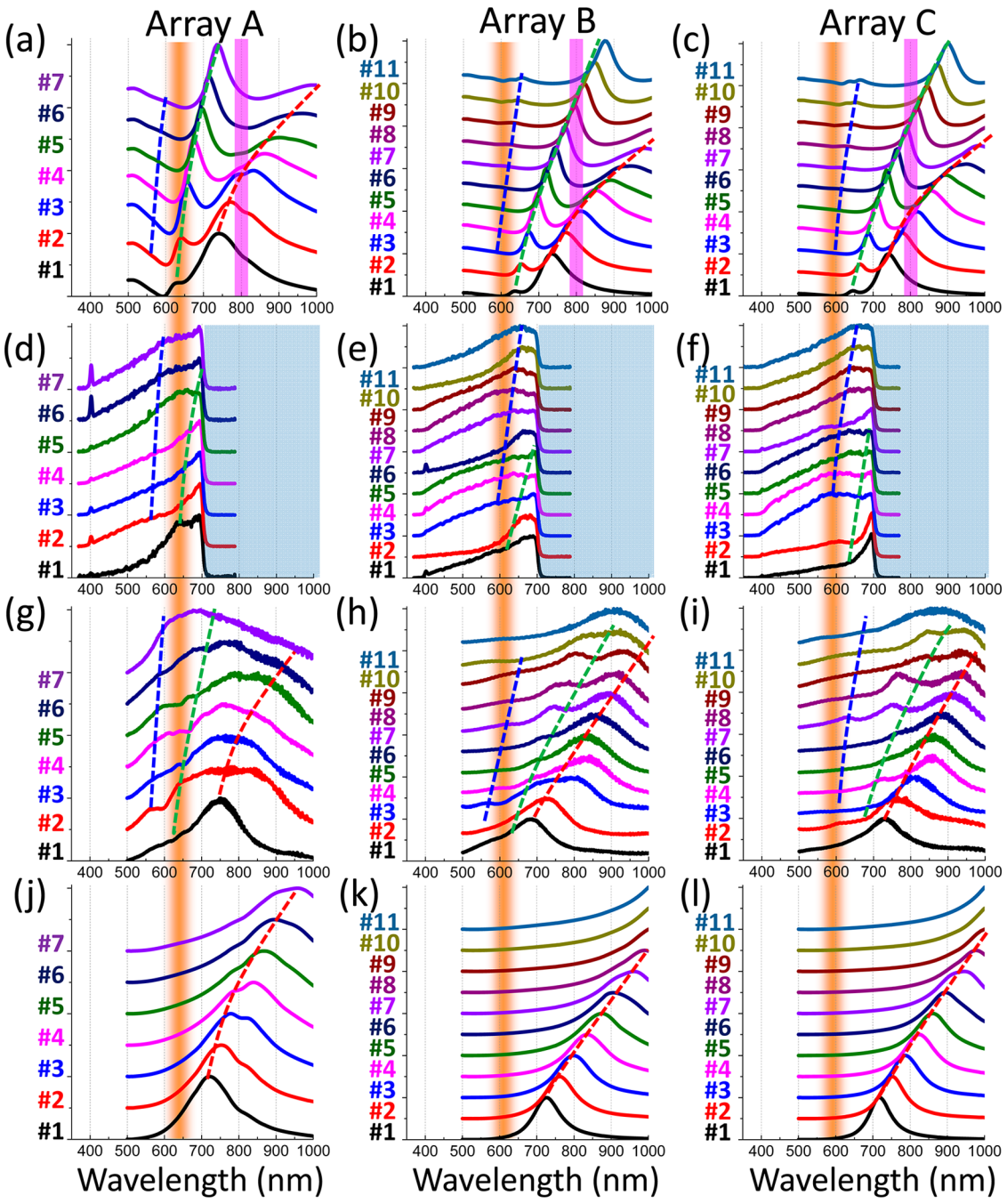

Figure 5. Longitudinal resonance spectra of nanoantennas in the three arrays obtained from simulated near-field intensity (a−c), experimental TPPL signals (d−f), experimental dark-field scattering (g−i), and simulated far-field scattering (j−l). The gradient orange area in each column marks the simulated transverse resonance shown in Figure 3. The magenta areas around 800 nm in (a-c) mark the laser excitation wavelength. The dashed lines in red, green, and blue colors are guide lines for the eye to the 1st order bonding, 1st order antibonding, and the 2nd order bonding modes, respectively. The gray areas in panels d−f are the spectral regime blocked by the short pass filter.

spectral feature are in good agreement with the scattering spectra obtained from dark-field experiments and numerical simulations.

The difference between the TPPL spectrum and the scattering spectrum occurs because the scattering spectrum is greatly dependent on the geometry of far-field excitation.[33] Differently, for the TPPL spectrum, the nanoantenna is excited by near-field dipole sources, that is, the electron−hole pairs in the gold arms. Therefore, almost all eigenmodes can be excited, and the TPPL spectrum reveals the emission properties of the nanoantenna. In other words, the TPPL spectrum reveals the ability of a nanoantenna to mediate the local e.m. energy to the far field, while the scattering spectrum involves both the far-to-near field and the near-to-far field coupling ability of a nanoantenna.

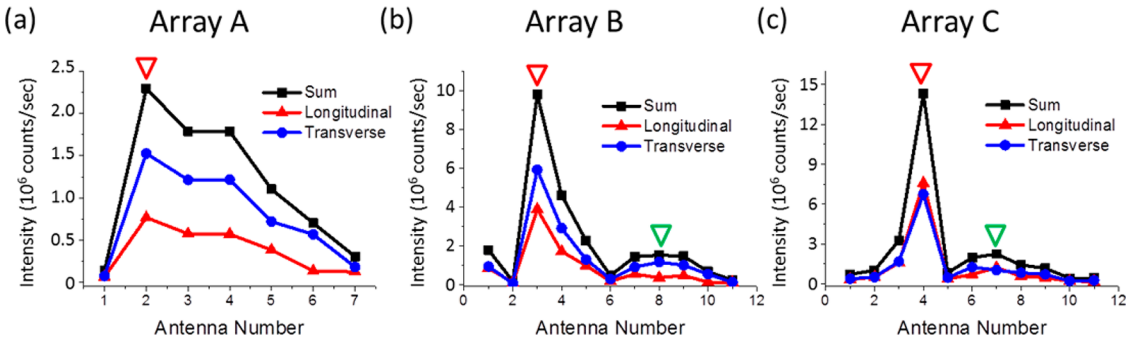

Figure 6. (a–c) Transverse (blue dots) and longitudinal (red triangles) TPPL intensity and the sum (black squares) as a functional of antenna number. Open triangles in red and green colors mark the intensity maxima due to the excitation of bonding and antibonding mode, respectively.

For our simple gap nanoantennas, the modulation effect of the antibonding and the nonfundamental longitudinal modes on the TPPL spectrum is not very pronounced due to the following possible reasons. The first step in the Au TPPL process is an intraband transition within the sp band of gold. This step requires a high field gradient to match the momentum.[17,21] Therefore, the TPPL generation is most efficient at the high-field gradient area inside the gold antenna arms. This means that the spatial distribution of the generated electron–hole pairs ("local TPPL dipoles") is determined by the field distribution of the excited resonant mode. On the other hand, for the local TPPL dipoles to decay into the nonfundamental resonant mode, they need to be present at spatial positions where the local density of optical states (LDOS) of the nonfundamental mode is not zero. In other words, for the TPPL to decay into antibonding or nonfundamental mode, the spatial distribution of the generated TPPL dipoles needs to overlap with that of the LDOS of the nonfundamental mode. Since the high-field gradient area of the fundamental mode is around the gap, it only partially overlaps with the spatial distribution of the LDOS of the antibonding or nonfundamental mode. As a result, only part of the generated TPPL dipoles can efficiently decay into the antibonding or the nonfundamental modes and the modulation effect is inherently not pronounced. For those TPPL dipoles that do not couple to the antibonding or the nonfundamental mode, they directly decay into typical TPPL emission without modulation. Such unmodulated TPPL then contributes to the background of our observed spectrum and further weakens the distinctiveness of the modulation features. To improve the distinctiveness of the modulation effect, the contribution from the unmodulated TPPL emission needs to be removed. We have acquired the TPPL spectrum from an extended gold film and used it to account for the contribution of the unmodulated TPPL. With such consideration, the visibility of the spectral features can be improved and the identification of the peaks/dips is more precise (see details and an example in the Supporting Information). To truly enhance the modulation effect, we suggest using more complex structures, such as a "dolmen-type" Fano resonator,[34,35] with which the coupling between the fundamental and nonfundamental modes can be optimized by engineering the structural geometry.

Influence of Resonant Modes on the TPPL Excitation Efficiency. Finally, we examine the role of antenna longitudinal resonant modes in the TPPL excitation. Figure 6 panels a–c show the TPPL intensities for each antenna in the three arrays recorded in transverse polarization (blue dots), in longitudinal polarization (red triangles), and the sum of the two polarization orientations (black squares). The excitation polarization is always kept parallel to the antenna's longitudinal axis. As the antenna length increases, the first bonding mode gradually red shifts and becomes in resonance with the laser excitation (marked by the magenta areas in Figure 5a–c), leading to the first maximum excitation efficiency of TPPL. Further increasing the antenna length red shifts the first antibonding mode into the laser excitation wavelength region. Once the symmetry of excitation is broken, subradiant antibonding modes can be excited. Since we are using a tightly focused laser spot to excite the antennas, the symmetry breaking is achieved automatically when the focal spot is displaced from the antenna's geometrical center. As a result, characteristic two-lobe patterns in the TPPL excitation map are observed when the antibonding mode is excited.[6] Such excitation then leads to the second maximum of the TPPL intensity. From the above analysis, we clearly see the effect of the first bonding and the first antibonding mode of symmetric nanoantennas on the excitation efficiency of TPPL. From the intensity scales of the three plots, we found that, under the same excitation power (100 μW on sample), thinner nanoantennas give higher TPPL yield compared to the thicker ones. This might be due to the relatively sharp geometrical variation in thinner antennas compared to that of the thicker ones. Another possible reason is the relatively complete field penetration (skin depth = 28 nm for gold at 800 nm) into the arm of the thin nanoantennas (height, width = 30 nm, 50 nm). Note that the

transverse TPPL is in general stronger than the longitudinal one because our observation window for TPPL is limited to the spectral range below 700 nm. Within this spectral window the transverse resonance-enhanced TPPL signals at the visible regime are more efficiently collected than the longitudinal ones. As can be seen from Figure 5, the longitudinal resonances of most nanoantennas fall into the near-infrared regime beyond the transmission window of our short pass filter.

CONCLUSION

We have studied the influence of resonant eigenmodes of optical nanoantennas on the two-photon photoluminescence of gold from the excited nanoantennas themselves. The transverse TPPL spectra show clear peaks shifting with the antenna's transverse resonance. For the longitudinal TPPL spectra, dips due to antibonding dark modes and slight enhancement by higher-order bonding mode are observed. The wavelength of the spectral feature is in good agreement with the data obtained from numerical simulations and dark-field scattering experiments. Previous work has attributed the spectral peaks in TPPL spectrum to the higher density of states near the X and L symmetry points of the first Brillouin zone of gold material.[36] However, our results show that the TPPL spectrum can be strongly reshaped by the nanostructure's resonant eigenmodes. Therefore, the lattice symmetry argument might need to take into account the resonance modes of the nanorod in order to obtain a more complete understanding of the spectral shape of TPPL. Our results also demonstrate the ability of nanoantennas to mediate the local electromagnetic energy to the far field and show that antenna resonance dominantly determines the spectral features of the TPPL from gold. The fact that the TPPL of gold is strongly depolarized and can be controlled by the nanoantenna also suggests potential applications of using TPPL as a controllable broadband local light source. Since the function of a nanoantenna depends on the actual mode in operation, the modulation effect of the resonant eigenmodes on the TPPL from the antennas offers a simple tool to characterize nanoantennas at their local environment.

MATERIALS AND METHODS

Dark-Field Microscope for Scattering Spectrum. To obtain a far-field scattering spectrum of single nanoantennas, we use a home-built dark-field setup (Figure S2a, Supporting Information). Nonpolarized light from a broadband white light source (HAL 100 illuminator with quartz collector, Zeiss) is concentrated onto the sample by an oil condenser (achromatic−aplanatic condenser, N.A. = 1.4, Zeiss). The scattered light is collected by an air objective (MPlanApo 60X air N.A.= 0.9, Olympus) on the opposite side of the condenser, and the collected light is aligned onto the entrance slit of a spectrometer (SR-303i-A with DU401A-BV CCD, Andor) with an achromatic lens (AC254-300-A-ML f = 300 mm, Thorlabs). A linear polarizer (LPVIS100-MP, 550−1500 nm, Thorlabs) is inserted before the achromatic lens to select the polarization of the scattering light.

Confocal Microscope for TPPL Spectrum. To excite the nanoantennas and acquire the TPPL, we use a home-built scanning laser confocal microscope equipped with a galvo-scanning mirror for the control of excitation position (Figure S2b, Supporting Information). Output from an infrared pulsed laser (central wavelength = 800 nm, pulse duration = 35 fs, repetition rate = 86 MHz, model TS Ti:sapphire laser kit, KMLabs) is reflected by a dichroic mirror (FF720-SDi01, Semrock) and focused onto the sample plane by an oil-immersion objective (100X S Fluor N.A. = 0.5−1.3 Oil Iris, Nikon). The averaged excitation power on the sample plane is 100 μW. The TPPL emission then passes through the dichroic mirror and a short pass filter (SP01-785RU-25, Semrock), which blocks light in the spectral regime above 700 nm and the straight scattering of the excitation laser. Finally, an analyzer selects the polarization of the TPPL before it is sent to a homemade spectrometer with a TE-cooled CCD detector (iDus DU420A-BU2, Andor) for spectroscopic analysis. In this work, we scan the excitation focal spot over the entire area of the antenna arrays and record the TPPL spectrum for each excitation position. The excitation laser is always linearly polarized along the longitudinal axis of the nanoantennas. To obtain the TPPL spectrum for each antenna, we perform a 10 × 10 spectral mapping covering an area less than 1 μm^2 around each antenna, and select the spectrum from the brightest spot in the TPPL spectral mapping image. The total TPPL intensity is obtained by integrating the intensity over the spectral widow ranging from 411 to 690 nm for the brightest spot pixel.

Numerical Simulations. 3D full-wave numerical simulations using the finite-difference time-domain method (FDTD Solutions, Lumerical Solutions) have been performed to gain qualitative understanding of the eigenmodes of the nanoantennas. Dimensions of nanoantennas obtained from the SEM images are used in the simulations. The thickness of the ITO layer is 40 nm. Experimental data are used for the optical properties of gold and ITO in the simulations.[37,38] For far-field scattering spectrum, a total-field scattered-field plane wave source[39] is used to excite the antenna from the glass substrate, mimicking the real experimental situation. All perfectly matched layer (PML) boundaries of the simulation volume are 1500 nm away from the antenna gap center. Such distance avoids the absorption of near fields by the PML boundaries. Mesh steps of the space discretization in x, y, and z directions are all set to be 2 nm within the volume covering a 500 × 500 × 500 nm^3 cubic space centered to the antenna gap center. Such a mesh step size allows the acquisition of satisfactory simulation accuracy within reasonable simulation time and memory. The scattering spectrum is obtained by plotting the scattered power as a function of wavelength. The scattered power is obtained by integrating the Poynting vector over the surface of a closed box consisting of six two-dimensional power monitors enclosing the nanoantenna. The closed box is centered to the antenna gap and has spans of 550, 250, and 250 nm in the x, y, and z directions, respectively. The transmission power has been normalized to the total source power and plotted as a function of the wavelength. The simulation setup is depicted in Figure S4a in the Supporting Information. As for near-field spectrum of an antenna, we use a Gaussian source illuminating the antenna from the glass half space, as shown in Figure S4b in the Supporting Information. The Gaussian beam is created by a thin lens set to have a numerical aperture of 1.4 using 200 plane waves, which provide sufficiently broad vector components for the numerical aperture.[39] To excite the antibonding mode, we have displaced the Gaussian beam from the geometrical center of the antenna such that the symmetry of the system is broken.[6] The near electric field intensity ($|E_x|^2 + |E_y|^2 + |E_z|^2$) recorded by a point monitor at a position 5 nm away from the antenna edge is plotted as a function of the wavelength. The mode assignment

is done by analyzing the near-field intensity distribution around the antenna arms at the wavelength of the resonance peak (Figure S5, Supporting Information).

Conflict of Interest: The authors declare no competing financial interest.

Acknowledgment. Support from the Ministry of Science and Technology (MOST) of Taiwan under Grant No. NSC-101-2113-M-007-002-MY2, NSC102-2119-M-002-015-MY3, and MOST-103-2113-M-007-004-MY3 are gratefully acknowledged. J.S.H. thanks the support from B. Hecht and the nanofabrication facilities at Wuerzburg University as well as the Center for Nanotechnology, Materials Sciences, and Microsystems at National Tsing Hua University.

Supporting Information Available: Images of structured flakes, microscope setups, TPPL spectra, FDTD simulations, mode assignment. This material is available free of charge *via* the Internet at http://pubs.acs.org.

REFERENCES AND NOTES

1. Novotny, L.; van Hulst, N. Antennas for Light. *Nat. Photonics* **2011**, *5*, 83–90.
2. Biagioni, P.; Huang, J.-S.; Hecht, B. Nanoantennas for Visible and Infrared Radiation. *Rep. Prog. Phys.* **2012**, *75*, 024402.
3. Chu, M.-W.; Myroshnychenko, V.; Chen, C. H.; Deng, J.-P.; Mou, C.-Y.; García de Abajo, F. J. Probing Bright and Dark Surface-Plasmon Modes in Individual and Coupled Noble Metal Nanoparticles Using an Electron Beam. *Nano Lett.* **2009**, *9*, 399–404.
4. Dorfmüller, J.; Vogelgesang, R.; Weitz, R. T.; Rockstuhl, C.; Etrich, C.; Pertsch, T.; Lederer, F.; Kern, K. Fabry–Pérot Resonances in One-Dimensional Plasmonic Nanostructures. *Nano Lett.* **2009**, *9*, 2373–2377.
5. Koh, A. L.; Bao, K.; Khan, I.; Smith, W. E.; Kothleitner, G.; Nordlander, P.; Maier, S. A.; McComb, D. W. Electron Energy-Loss Spectroscopy (EELS) of Surface Plasmons in Single Silver Nanoparticles and Dimers: Influence of Beam Damage and Mapping of Dark Modes. *ACS Nano* **2009**, *3*, 3015–3022.
6. Huang, J.-S.; Kern, J.; Geisler, P.; Weinmann, P.; Kamp, M.; Forchel, A.; Biagioni, P.; Hecht, B. Mode Imaging and Selection in Strongly Coupled Nanoantennas. *Nano Lett.* **2010**, *10*, 2105–2110.
7. Davis, T. J.; Gómez, D. E.; Vernon, K. C. Simple Model for the Hybridization of Surface Plasmon Resonances in Metallic Nanoparticles. *Nano Lett.* **2010**, *10*, 2618–2625.
8. Dorfmüller, J.; Vogelgesang, R.; Khunsin, W.; Rockstuhl, C.; Etrich, C.; Kern, K. Plasmonic Nanowire Antennas: Experiment, Simulation, and Theory. *Nano Lett.* **2010**, *10*, 3596–3603.
9. Alber, I.; Sigle, W.; Müller, S.; Neumann, R.; Picht, O.; Rauber, M.; van Aken, P. A.; Toimil-Molares, M. E. Visualization of Multipolar Longitudinal and Transversal Surface Plasmon Modes in Nanowire Dimers. *ACS Nano* **2010**, *5*, 9845–9853.
10. Taminiau, T. H.; Stefani, F. D.; van Hulst, N. F. Optical Nanorod Antennas Modeled as Cavities for Dipolar Emitters: Evolution of Sub- and Super-radiant Modes. *Nano Lett.* **2011**, *11*, 1020–1024.
11. Schuck, P. J.; Fromm, D. P.; Sundaramurthy, A.; Kino, G. S.; Moerner, W. E. Improving the Mismatch between Light and Nanoscale Objects with Gold Bowtie Nanoantennas. *Phys. Rev. Lett.* **2005**, *94*, 017402.
12. Kinkhabwala, A.; Yu, Z.; Fan, S.; Avlasevich, Y.; Müllen, K.; Moerner, W. E. Large Single-Molecule Fluorescence Enhancements Produced by a Bowtie Nanoantenna. *Nat. Photonics* **2009**, *3*, 654–657.
13. Liu, W.-L.; Lin, F.-C.; Yang, Y.-C.; Huang, C.-H.; Gwo, S.; Huang, M. H.; Huang, J.-S. The Influence of Shell Thickness of Au@TiO_2 Core–Shell Nanoparticles on The Plasmonic Enhancement Effect in Dye-Sensitized Solar Cells. *Nanoscale* **2013**, *5*, 7953–7962.
14. Gallinet, B.; Martin, O. J. F. Influence of Electromagnetic Interactions on the Line Shape of Plasmonic Fano Resonances. *ACS Nano* **2011**, *5*, 8999–9008.
15. Ye, J.; Wen, F.; Sobhani, H.; Lassiter, J. B.; van Dorpe, P.; Nordlander, P.; Halas, N. J. Plasmonic Nanoclusters: Near Field Properties of the Fano Resonance Interrogated with SERS. *Nano Lett.* **2012**, *12*, 1660–1667.
16. Beversluis, M. R.; Bouhelier, A.; Novotny, L. Continuum Generation from Single Gold Nanostructures through Near-Field Mediated Intraband Transitions. *Phys. Rev. B* **2003**, *68*, 115433.
17. Biagioni, P.; Celebrano, M.; Savoini, M.; Grancini, G.; Brida, D.; Mátéfi-Tempfli, S.; Mátéfi-Tempfli, M.; Duò, L.; Hecht, B.; Cerullo, G.; *et al.* Dependence of The Two-Photon Photoluminescence Yield of Gold Nanostructures on The Laser Pulse Duration. *Phys. Rev. B* **2009**, *80*, 045411.
18. Wissert, M. D.; Ilin, K. S.; Siegel, M.; Lemmer, U.; Eisler, H.-J. Coupled Nanoantenna Plasmon Resonance Spectra from Two-Photon Laser Excitation. *Nano Lett.* **2010**, *10*, 4161–4165.
19. Castro-Lopez, M.; Brinks, D.; Sapienza, R.; van Hulst, N. F. Aluminum for Nonlinear Plasmonics: Resonance-Driven Polarized Luminescence of Al, Ag, and Au Nanoantennas. *Nano Lett.* **2011**, *11*, 4674–4678.
20. Wissert, M. D.; Moosmann, C.; Ilin, K. S.; Siegel, M.; Lemmer, U.; Eisler, H.-J. Gold Nanoantenna Resonance Diagnostics *via* Transversal Particle Plasmon Luminescence. *Opt. Exp.* **2011**, *19*, 3686–3693.
21. Biagioni, P.; Brida, D.; Huang, J.-S.; Kern, J.; Duò, L.; Hecht, B.; Finazzi, M.; Cerullo, G. Dynamics of Four-Photon Photoluminescence in Gold Nanoantennas. *Nano Lett.* **2012**, *12*, 2941–2947.
22. Schwab, P. M.; Moosmann, C.; Wissert, M. D.; Schmidt, E. W.-G.; Ilin, K. S.; Siegel, M.; Lemmer, U.; Eisler, H.-J. Linear and Nonlinear Optical Characterization of Aluminum Nanoantennas. *Nano Lett.* **2013**, *13*, 1535–1540.
23. Guan, Z.; Gao, N.; Jiang, X.-F.; Yuan, P.; Han, F.; Xu, Q.-H. Huge Enhancement in Two-Photon Photoluminescence of Au Nanoparticle Clusters Revealed by Single-Particle Spectroscopy. *J. Am. Chem. Soc.* **2013**, *135*, 7272–7277.
24. Ghenuche, P.; Cherukulappurath, S.; Taminiau, T. H.; van Hulst, N. F.; Quidant, R. Spectroscopic Mode Mapping of Resonant Plasmon Nanoantennas. *Phys. Rev. Lett.* **2008**, *101*, 116805.
25. Dulkeith, E.; Niedereichholz, T.; Klar, T. A.; Feldmann, J.; Von Plessen, G.; Gittins, D. I.; Mayya, K. S.; Caruso, F. Plasmon Emission in Photoexcited Gold Nanoparticles. *Phys. Rev. B* **2004**, *70*, 205424.
26. Yorulmaz, M.; Khatua, S.; Zijlstra, P.; Gaiduk, A.; Orrit, M. Luminescence Quantum Yield of Single Gold Nanorods. *Nano Lett.* **2012**, *12*, 4385–4391.
27. Hu, H.; Duan, H.; Yang, J. K. W.; Shen, Z. X. Plasmon-Modulated Photoluminescence of Individual Gold Nanostructures. *ACS Nano* **2012**, *6*, 10147–10155.
28. Huang, J.-S.; Callegari, V.; Geisler, P.; Brüning, C.; Kern, J.; Prangsma, J. C.; Wu, X.; Feichtner, T.; Ziegler, J.; Weinmann, P.; *et al.* Atomically Flat Single-Crystalline Gold Nanostructures for Plasmonic Nanocircuitry. *Nature Comm.* **2010**, *1*, 150.
29. Wang, Y.; Abb, M.; Boden, S. A.; Aizpurua, J.; De Groot, C. H.; Muskens, O. L. Ultrafast Nonlinear Control of Progressively Loaded, Single Plasmonic Nanoantennas Fabricated Using Helium Ion Milling. *Nano Lett.* **2013**, *13*, 5647–5653.
30. Kollmann, H.; Piao, X.; Esmann, M.; Becker, S. F.; Hou, D.; Huynh, C.; Kautschor, L.-O.; Bösker, G.; Vieker, H.; Beyer, A.; *et al.* Toward Plasmonics with Nanometer Precision: Nonlinear Optics of Helium-Ion Milled Gold Nanoantennas. *Nano Lett.* **2014**, *14*, 4778–4784.
31. Ringe, E.; Langille, M. R.; Sohn, K.; Zhang, J.; Huang, J.; Mirkin, C. A.; Van Duyne, R. P.; Marks, L. D. Plasmon Length: A Universal Parameter To Describe Size Effects in Gold Nanoparticles. *J. Phys. Chem. Lett.* **2012**, *3*, 1479–1483.
32. Bryant, G. B.; García de Abajo, F. J.; Aizpurua, J. Mapping the Plasmon Resonances of Metallic Nanoantennas. *Nano Lett.* **2008**, *8*, 631–636.
33. Fan, J. A.; Bao, K.; Lassiter, J. B.; Bao, J.; Halas, N. J.; Nordlander, P.; Capasso, F. Near-Normal Incidence Dark-Field Microscopy: Applications to Nanoplasmonic Spectroscopy

Mapping the Plasmon Resonances of Metallic Nanoantennas. *Nano Lett.* **2012**, *12*, 2817–2821.
34. Zhang, S.; Genov, D. A.; Wang, Y.; Liu, M.; Zhang, X. Plasmon-Induced Transparency in Metamaterials. *Phys. Rev. Lett.* **2008**, *101*, 047401.
35. Verellen, N.; Sonnefraud, Y.; Sobhani, H.; Hao, F.; Moshchalkov, V. V.; Van Dorpe, P.; Nordlander, P.; Maier, S. A. Fano Resonances in Individual Coherent Plasmonic Nanocavities. *Nano Lett.* **2009**, *9*, 1663–1667.
36. Imura, K.; Nagahara, T.; Okamoto, H. Plasmon Mode Imaging of Single Gold Nanorods. *J. Am. Chem. Soc.* **2004**, *126*, 12730–12731.
37. Johnson, P. B.; Christy, R. W. Optical Constants of the Noble Metals. *Phys. Rev. B* **1972**, *6*, 4370–4379.
38. Laux, S.; Kaiser, N.; Zöller, A.; Götzelmann, R.; Lauth, H.; Bernitzki, H. Room-Temperature Deposition of Indium Tin Oxide Thin Films with Plasma Ion-Assisted Evaporation. *Thin Solid Films* **1998**, *335*, 1–5.
39. *Lumerical Solutions Knowledge Base*; release 2014a; Lumerical Solutions: Vancouver, Canada, 2014; http://docs.lumerical.com/en/ref_sim_obj_sources.html.